

Probing stochastic inter-galactic magnetic fields using blazar-induced gamma ray halo morphology

Francis Duplessis* and Tanmay Vachaspati*†

**Physics Department, Arizona State University, Tempe, AZ 85287, USA.*

†*Maryland Center for Fundamental Physics, University of Maryland, College Park, MD 20742, USA.*

Inter-galactic magnetic fields can imprint their structure on the morphology of blazar-induced gamma ray halos. We show that the halo morphology arises through the interplay of the source’s jet and a two-dimensional surface dictated by the magnetic field. Through extensive numerical simulations, we generate mock halos created by stochastic magnetic fields with and without helicity, and study the dependence of the halo features on the properties of the magnetic field. We propose a sharper version of the Q-statistics and demonstrate its sensitivity to the magnetic field strength, the coherence scale, and the handedness of the helicity. We also identify and explain a new feature of the Q-statistics that can further enhance its power.

I. INTRODUCTION

Multiple analyses of observed gamma rays [1–7] provide growing evidence for the existence of inter-galactic magnetic fields (for reviews see [8, 9]). The existence of such magnetic fields poses new questions for cosmology and probably also for particle physics [10, 11]. In addition, a primordial magnetic field can play an important role during structure formation in the universe and could help us understand the ubiquity of magnetic fields in astrophysical bodies.

A critical challenge at this stage is to sharpen observational techniques so that we can better observe and measure inter-galactic magnetic fields. Of the various probes of inter-galactic magnetic fields, blazar-induced gamma ray cascades hold certain key advantages. The gamma ray cascades originate in the voids in the large-scale structure and are mostly immune to complications of a noisy environment. The cascade develops in a relatively small spatial volume and hence is a local probe of the magnetic field in the voids. This is distinct from other methods, such as the Faraday rotation of the cosmic microwave background polarization, that probe an integrated measure of the magnetic field. Gamma ray cascades are also highly sensitive probes and can trace very weak cosmological magnetic fields.

In this paper we study the effect of stochastic inter-galactic magnetic fields on blazar induced gamma ray halos and some results overlap with those of Refs. [12–16]. The cascade process is complicated and all analyses use some simplifying assumptions. For example, the analysis in Ref. [13] only considered non-stochastic magnetic field configurations. Other simplification schemes, such as the “large spherical observer” method employed in Ref. [14], transport arrival directions of gamma rays for distant observers to a single Earth-bound observer. This technique is certainly useful to study spectral properties of the cascade, but there is a danger that it loses or shuffles the spatial information of gamma ray arrival directions that is crucial for morphological studies. Our focus is on the effect of stochastic magnetic fields that are statistically isotropic and with or without helicity.

So we carefully analyse the spatial information of the gamma rays that is useful for deducing properties of the magnetic field but, for the present, we only include an approximate description of the cascade development.

An important helpful concept that we develop in this paper is that of the “PP surface” (see Sec. III). This spatial surface holds the key to halo morphology and many of the features that we see in our simulations can be understood in terms of the shape of the PP surface and its intersection with the blazar jet.

We have applied a refined version of the Q-statistics first proposed in Ref. [17] to study the morphology of halos. Our results show that this statistic can successfully extract the helicity of the magnetic field. Our simulations also reveal that the plot of $Q(R)$, where R is a variable that will be explained below, has an additional bump. We are able to show that this bump is a genuine feature of the Q-statistic and explain it in terms of properties of the PP surface in Sec. VII. Thus this extra feature of $Q(R)$ may become an observational tool in future.

We give some background information in Sec. II, discuss our simulation techniques in Sec. III, discuss features of the halo in Sec. IV, present results with non-stochastic fields in Sec. V and with stochastic fields in Sec. VI. As mentioned above, we discuss the bump feature in $Q(R)$ in Sec. VII. We summarize our conclusions in Sec. VIII. Our stochastic magnetic field generation scheme is described in Appendix A.

II. BLAZAR HALOS FROM AN INTERGALACTIC MAGNETIC FIELD

TeV photons from blazars induced electromagnetic cascades through pair production with the extragalactic background light, $\gamma_{\text{EBL}} \gamma_{\text{TeV}} \rightarrow e^+ e^-$. In the presence of a magnetic field, the charged leptons follow spiral paths as they propagate and lose energy due to inverse Compton scattering with the cosmic microwave background (CMB) photons. The up-scattered CMB photons have gamma ray energies and produce extended halos around the direction of the blazar. In this section we briefly discuss

the formation of the halo under simplifying assumptions.

Consider a blazar located at the origin of our coordinate system described by the unit basis vectors $\hat{\mathbf{x}}, \hat{\mathbf{y}}, \hat{\mathbf{z}}$. We choose $\hat{\mathbf{z}}$ so that Earth is located at $\mathbf{r}_E = -d_s \hat{\mathbf{z}}$ where d_s is the comoving distance to the source,

$$d_s = \frac{1}{a_0 H_0} \int_0^{z_s} \frac{1}{\sqrt{\Omega_m(1+z)^3 + \Omega_\Lambda}} dz \simeq \frac{z_s}{0.22} \text{Gpc}. \quad (1)$$

To perform the integral, we have used $\Omega_\Lambda \approx 0.69$, $\Omega_m \approx 0.31$, $H_0 \approx 0.67h$ as found in Ref. [18] and we have also assumed that $z_s \ll 1$ and used natural units so that $c = 1$. For all the simulations in this paper we will choose $d_s = 1$ Gpc.

The blazar will typically emit photons in a collimated jet which we approximate to be a conical region with half-opening angle $\theta_{\text{jet}} \approx 5^\circ$. The energy $E_{\gamma 0}$ of these photons must lie above some threshold of about a TeV if they are to produce an electron-positron pair from interaction with the Extragalactic Background Light (EBL). Due to the opacity of the EBL, the TeV photons will travel a mean free path (MFP) determined by the pair production cross section $\omega_{\gamma\gamma}$ and the number density of the EBL photons n_{EBL} ,

$$D_{\gamma 0} = \langle \sigma_{\gamma\gamma} n_{\text{EBL}} \rangle^{-1} \simeq (80 \text{Mpc}) \frac{\kappa}{(1+z_{\gamma\gamma})^2} \left(\frac{10 \text{TeV}}{E_{\gamma 0}} \right), \quad (2)$$

We have assumed that $n_{\text{EBL}} \propto (1+z_{\gamma\gamma})^{-2}$ to approximate the MFP in the final equality [19]. Following [13] we will set $\kappa = 1$ as this dimensionless constant is estimated to lie in the range of $0.3 < \kappa < 3$. The comoving distance from the source to the pair production event is given by $D_{\gamma 0}^c = (1+z_{\gamma\gamma})D_{\gamma 0}$.

The redshift of the produced lepton pairs will depend on the relative position of the leptons to the source. Since $D_{\gamma 0}^c \ll d_s$, we make the approximation $z_{\gamma\gamma} \approx z_s$ and we can write,

$$D_{\gamma 0}^c \simeq (80 \text{Mpc}) \frac{\kappa}{(1+z_s)} \left(\frac{10 \text{TeV}}{E_{\gamma 0}} \right). \quad (3)$$

The energy of each of the produced leptons will be $E_e \approx E_{\gamma 0}/2$. These leptons are expected to travel a distance D_e before losing most of their energy through inverse Compton (IC) cooling which occurs by upscattering CMB photons. The cooling distance is

$$D_e = \frac{3m_e^2}{4\sigma_T U_{\text{CMB}} E_e} \simeq (31 \text{kpc}) \left(\frac{5 \text{TeV}}{E_e} \right) \left(\frac{1.22}{1+z_{\gamma\gamma}} \right)^4 \quad (4)$$

where $\sigma_T = 6.65 \times 10^{-25} \text{cm}^2$ is the Thomson scattering cross section and $U_{\text{CMB}}(z_{\gamma\gamma}) \simeq (0.26 \text{eV/cm}^3)(1+z_{\gamma\gamma})^4$ is the CMB energy density. Note that we can assume the whole cascade development happens around redshift $z_{\gamma\gamma}$ as $D_e \ll D_{\gamma 0}$. At that redshift, the average energy of a CMB photon is

$$E_{\text{CMB}} \simeq (6 \times 10^{-4} \text{eV})(1+z_{\gamma\gamma}), \quad (5)$$

which implies that, from energy conservation, the upscattered photons will have energy

$$E_\gamma = \frac{4}{3} E_{\text{CMB}} \frac{E_e^2}{m_e^2} \simeq (77 \text{GeV}) \left(\frac{E_{\gamma 0}}{10 \text{TeV}} \right)^2. \quad (6)$$

As the lepton propagates, it upscatters $\approx (10 \text{TeV})/(10 \text{GeV}) \sim 10^3$ photons, and produces a gamma ray cascade in the 1-100 GeV range if the initial gamma ray had an energy of a few TeV. Clearly not every photon upscattered by the leptons will reach Earth. Those that do must come from a set of events that satisfy a set of three constraints given in Ref. [13] that we now describe.

After pair production, the lepton's initial velocity will be almost parallel to the momentum of the parent photon with a negligible deviation of order the inverse Lorentz boost factor $m_e/E_e \sim 10^{-6}$. Their subsequent trajectory will be determined by the magnetic field $\mathbf{B}(\mathbf{x})$ through the Lorentz force. If the magnetic field is incoherent on length scales smaller than the cooling distance $D_e \sim 30 \text{kpc}$, the lepton trajectories will be diffusive and this situation is much harder to analyze. So we focus on magnetic fields that are coherent on scales that are much larger than D_e . Then the lepton trajectories are bent in an effectively constant magnetic field and follow a helical trajectory with gyroradius

$$R_L = R_{L0} |\mathbf{v}_\perp|, \quad \text{with } R_{L0} = \frac{E_e}{e|\mathbf{B}|}, \quad (7)$$

which depends on the lepton's perpendicular velocity to \mathbf{B} , *i.e.* $\mathbf{v}_\perp = \mathbf{v} - (\mathbf{v} \cdot \hat{\mathbf{B}})\hat{\mathbf{B}}$.

The quantity $2\pi R_{L0}$ is useful as it denotes the distance the lepton must travel in order to perform a full revolution. The value of R_{L0} is a function of the redshift as it depends on $|\mathbf{B}|$. For magnetic fields frozen in the plasma, the field strength redshifts as $|\mathbf{B}| = B_0(1+z_{\gamma\gamma})^2 \approx B_0(1+z_s)^2$ where B_0 is the magnetic field magnitude today. With

$$R_{L0} \simeq 3.5 \text{Mpc} \left(\frac{E_e}{5 \text{TeV}} \right) \left(\frac{B_0}{10^{-15} \text{G}} \right)^{-1} \left(\frac{1+z_s}{1.22} \right)^{-2}, \quad (8)$$

we can evaluate the ratio

$$\frac{D_e}{2\pi R_{L0}} \simeq 0.0106 \left(\frac{E_\gamma}{10 \text{GeV}} \right)^{-1} \left(\frac{B_0}{10^{-15} \text{G}} \right) \left(\frac{1+z_s}{1.22} \right)^{-2} \quad (9)$$

which determines the angular deflection of the leptons.

As depicted in Fig. 1, let us introduce the following angles: θ is the arrival angle of the GeV photon with respect to the source location, δ represents the angle between the upscattered photon and the TeV photon, α is the angle subtended by the TeV photon's momentum, \mathbf{r}_E the vector from the source to Earth, and finally ϕ is the azimuthal angle in which the whole (planar) scattering process take place. We also introduce the polar vectors $\hat{\boldsymbol{\rho}}$ and $\hat{\boldsymbol{\phi}}$, in the $\hat{\mathbf{x}}, \hat{\mathbf{y}}$ plane. It is important to emphasize that the whole process occurs in a plane to a good approximation because $D_e \ll D_{\gamma 0}^c, d_s$ and the length of the

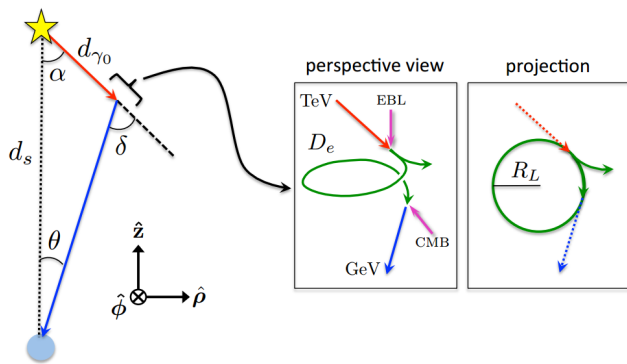


FIG. 1: A TeV photon emitted from a blazar travels a comoving distance of $d_{\gamma 0}$ before scattering off an EBL photon and pair producing leptons. The lepton trajectories are bent due to the local magnetic field over a very short distance compared to the distance to the source, d_s , and are shown in the insets. (The insets show huge bending whereas we have only considered magnetic fields that give small bending.) Inverse-Compton scattering of a lepton and CMB photons results in a cascade of GeV energy gamma rays arriving at Earth from the direction of the pair production. [Sketch taken from [13].]

lepton trajectory can be ignored. Then there are only 3 points that are relevant (the source, the pair production point, and the observer) and they always lie in a plane.

Applying the sine formula to the triangle in Fig. 1 we get our first constraint

$$d_s \sin(\theta) = d_{\gamma 0} \sin(\delta). \quad (10)$$

where $d_{\gamma 0}$ is the distance traveled by the TeV photon and is a random variable drawn from a distribution that depends on the MFP $D_{\gamma 0}^c$ in Eq. (3). This is discussed in detail in Sec. III.

The bending angle δ is related to the distance traveled by the lepton through the local magnetic field which we write as $\mathbf{B} = B\hat{\mathbf{n}}_{\parallel}$. We also decompose the lepton's initial velocity at time $t_i = 0$, $\mathbf{v}(t_i = 0) = v_{\parallel}\hat{\mathbf{n}}_{\parallel} + v_{\perp}\hat{\mathbf{n}}_{\perp}$, where $\hat{\mathbf{n}}_{\perp} \cdot \hat{\mathbf{n}}_{\parallel} = 0$. At some later time t the velocity is

$$\mathbf{v}(t) = v_{\parallel}\hat{\mathbf{n}}_{\parallel} + v_{\perp} \cos(\omega t)\hat{\mathbf{n}}_{\perp} \pm v_{\perp} \sin(\omega t)(\hat{\mathbf{n}}_{\perp} \times \hat{\mathbf{n}}_{\parallel}), \quad (11)$$

Here we introduced the angular frequency of the orbital motion $\omega = v_{\perp}/R_L = 1/R_{L0}$ and the $+$ ($-$) sign refers to the positron (electron) trajectory. A CMB photon upscattered at time t_{IC} will be directed along the lepton's trajectory and so the deflection angle of Figure 1 can be expressed as $\cos(\delta) = \hat{\mathbf{v}}(0) \cdot \hat{\mathbf{v}}(t_{IC})$. Using Eq. (11) we can derive the second constraint,

$$1 - \cos(\delta) = \left(1 - (\hat{\mathbf{v}}(0) \cdot \hat{\mathbf{B}})^2\right) \left(1 - \cos(t_{IC}/R_{L0})\right). \quad (12)$$

The time of inverse Compton scattering t_{IC} is a stochastic variable. Given its value and the magnetic field direction, the constraints determine the bending angle, δ .

A single propagating lepton will be able to upscatter CMB photons towards Earth only at certain times when the lepton's momentum is directed towards Earth. Photons upscattered at other times will not reach Earth and we can safely ignore them. The number of photons upscattered by a lepton is very large ($\sim 10^3$), with mean deviation angles between the photons $\sim 10^{-3} \times 0.01$ (see Eq. (9)). This angle is large enough that we only expect ~ 1 of the cascade photons from any lepton to reach Earth. This allows us to adopt the strategy that we first select a value of t_{IC} from an exponential probability distribution as described in Sec. III and then solve the constraint equations to find all TeV gamma rays from the blazar that upscatter CMB photons that reach Earth. For different values of t_{IC} , different TeV gamma rays from the blazar will lead to observed photons. In this way, we will be able to track the photons that arrive on Earth and not waste computational effort on those that go elsewhere.

The third and final constraint is that the cascade gamma ray lies in the plane specified by $\hat{\phi}$. This requires that the Lorentz force in the azimuthal $\hat{\phi}$ direction vanishes between the time of pair production and IC scattering. Namely the ϕ component of the impulse must vanish,

$$J_{\phi} = \hat{\phi} \cdot \mathbf{J} = \hat{\phi} \cdot \left(\pm e \int_0^{t_{IC}} dt \mathbf{v}(t) \times \mathbf{B} \right) = 0. \quad (13)$$

The impulse can be simplified by pulling out the assumed constant magnetic field of the integral and defining

$$\mathbf{v}_{\text{avg}} = \frac{1}{t_{IC}} \int_0^{t_{IC}} dt \mathbf{v}(t). \quad (14)$$

The geometrical setup of Fig. 1 forces \mathbf{v}_{avg} to bisect the angle δ and therefore its unit vector can be written as

$$\hat{\mathbf{v}}_{\text{avg}} = \sin(\delta/2 - \theta)\hat{\rho} - \cos(\delta/2 - \theta)\hat{\mathbf{z}}. \quad (15)$$

Decomposing \mathbf{B} as

$$\mathbf{B} = b_{\rho}\hat{\rho} + b_{\phi}\hat{\phi} + b_z\hat{\mathbf{z}} \quad (16)$$

allows us to write

$$\hat{\phi} \cdot \hat{\mathbf{v}}_{\text{avg}} \times \hat{\mathbf{B}} = -b_{\rho} \cos(\delta/2 - \theta) - b_z \sin(\delta/2 - \theta) = 0. \quad (17)$$

To summarize this section, Eqs. (10), (12) and (17) are the constraints that need to be satisfied by the variables (θ, δ, ϕ) given a magnetic field realization and initial velocity of the TeV gamma ray (both of which depend on (θ, δ, ϕ)), the source-observer distance (d_s), the distance to pair production ($d_{\gamma 0}$), and the photon upscattering time (t_{IC}).

III. HALO SIMULATIONS

For events that satisfy the constraints in Eqs. (10), (12) and (17), an observer on Earth will receive flux at a polar

angle of θ from the line of sight (LoS) to the blazar and at an azimuthal angle ϕ . It is possible to solve for these angles analytically in certain regimes for specific magnetic fields $\mathbf{B}(\mathbf{x})$ while using the MFPs of the particles: $t_{IC} = D_e$ as given by Eq. (4) and $D_{\gamma 0}^c$ as given in Eq. (3) [13]. We will refer to these values as “canonical” propagating distances (PDs), in contrast to the “stochastic” PDs we will use later. Numerical methods are required when considering more general $\mathbf{B}(\mathbf{x})$ and when including the stochasticity in the PDs of the initial gamma ray and pair produced leptons. Note that $D_e, D_{\gamma 0}^c$ depend on the energy E_γ of the final gamma ray reaching Earth. Therefore, in the analysis with canonical PDs, once we specify $\mathbf{B}(\mathbf{x})$ we can expect to find a 1 dimensional curve $\theta(E_\gamma), \phi(E_\gamma)$ by solving the constraints. The analysis with the canonical PDs is helpful because it gives an idea of the overall shape that the extended emission will resemble even when we include stochasticity.

For the case of stochastic PD the constraint equations are solved with $d_e = t_{IC}$ drawn from the probability density function

$$P[d_e] = \frac{1}{D_e} e^{-d_e/D_e} \quad (18)$$

and similarly the distance $d_{\gamma 0}$ traversed by a TeV gamma ray is drawn from

$$P[d_{\gamma 0}] = \frac{1}{D_{\gamma 0}^c} e^{-d_{\gamma 0}/D_{\gamma 0}^c}. \quad (19)$$

We will solve the constraint equations in a variety of magnetic field backgrounds, starting with simple analytic configurations for illustration purposes, and then move on to the more realistic case of stochastic, isotropic magnetic fields. Our procedure to generate stochastic, isotropic magnetic fields is described in Appendix A.

Turning to the energy distribution of gamma rays in our simulations, we assume a power law for the blazar spectrum [20, 21] and follow Ref. [15] by choosing a spectral index of $\Gamma \simeq 2.5$ that is characteristic of the TeV sources. This yields a spectrum given by,

$$\frac{dN_{\gamma 0}}{dE_{\gamma 0}} \sim \left(\frac{E_{\gamma 0}}{\text{TeV}} \right)^{-2.5}. \quad (20)$$

We can use the relation between $E_{\gamma 0}$ and E_γ to turn the blazar spectrum into one for the observed photons

$$\frac{dN_\gamma}{dE_\gamma} \sim \left(\frac{E_\gamma}{\text{TeV}} \right)^{-1.75}. \quad (21)$$

Our simulation algorithm proceeds in the following steps. First we draw an observed energy, E_γ , from the distribution in Eq. (21). The drawn value of E_γ determines the energy of the high energy photon, $E_{\gamma 0}$, from Eq. (6). With the values of E_γ and $E_{\gamma 0}$ we can find $D_{\gamma 0}^c$ and D_e from Eqs. (3) and (4), then use Eqs. (18) and (19) to draw values of $d_e = t_{IC}$ and $d_{\gamma 0}$. Now we

try to solve the constraint equations (10), (12) and (17). If a solution does not exist we go back to the first step and draw an observed energy E_γ . If a solution does exist, it gives the coordinates (θ, δ, ϕ) of an event on Earth at energy E_γ that satisfies all the constraints. We repeat the entire process until 1000 solutions are found. For a jet source, we only retain the events whose initial TeV photon lie within the jet. These small number of events give us the observed halo that will be shown in our plots.

To start we consider a source that radiates TeV photons isotropically in two different magnetic field backgrounds. The first background,

$$\mathbf{B} = B_0 \left(\cos(\beta) \hat{\mathbf{y}} - \sin(\beta) \hat{\mathbf{z}} \right), \quad (22)$$

with $\beta = \pi/4$, is a uniform magnetic field pointing at an angle $\pi/4$ from the line of sight. The second background is a maximally helical field

$$\mathbf{B} = B_0 \left(\sin(2\pi x/\lambda) \hat{\mathbf{x}} + \cos(2\pi x/\lambda) \hat{\mathbf{y}} \right). \quad (23)$$

Here λ is the coherence length of the helical field. We will take $d_s = 1$ Gpc, $B_0 = 10^{-14}$ G and $\lambda = 250$ Mpc as the prototypical values and eventually vary them one at a time to see their effect on the halo morphology.

Next we solve the constraint equations with the canonical PDs and determine the arrival directions θ, ϕ for several different energies, E_γ , for an isotropically emitting source. With canonical PDs, the events lie on a one dimensional curve shown in Fig. 2 in black. The corresponding simulations with stochastic PDs results in the distribution of points in Fig. 2. The points at lower energies are located further away from the source direction as is to be expected since the TeV gamma ray travels further at low energies before pair producing leptons (Eq. (3)) and leptons at low energies bend more before up-scattering CMB photons (Eq. (9)). Looking closely at Fig. 2, the drawn points are triangular; upright triangles are gamma rays that originate from electrons and inverted triangles are those that originate from positrons. The distinction is made clearer in Fig. 3 where red (black) points originate from positron (electron) processes. If the source was taken to be a jet, gamma rays predominantly from one of the two leptons will be observed.

The constraint equations are quite complicated to solve but there is a helpful visualization. First consider the third constraint equation, Eq. (17), and note that b_ρ and b_ϕ are also functions of θ, δ and ϕ . So Eq. (17) provides one functional relation between these variables that only depends on the magnetic field background. Hence the magnetic field defines a two-dimensional surface in space. We will call this the “Pair Production surface” or the “PP surface” since only lepton pair production at this surface can send GeV gamma rays to the observer. In Fig. 4 we show the PP surface for the magnetic fields of Eqs. (22) and (23). On these plots we also show the

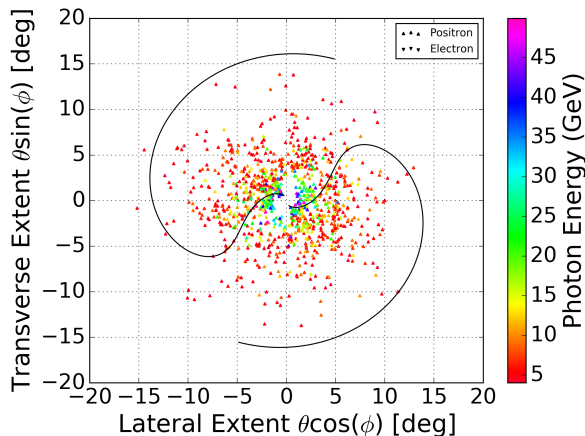
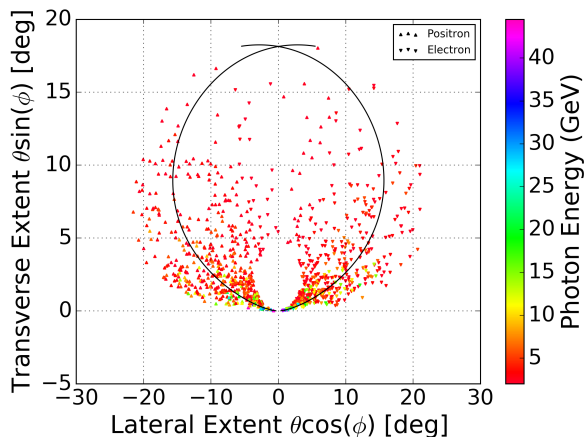


FIG. 2: Example of halos from blazars in a uniform (top) and maximally helical (bottom) inter-galactic magnetic field as given in Eqs. (22) and (23) [13]. The colors denote the energy of the observed gamma ray.

pair production locations, “PP locations”, that resulted in the halos of Fig. 2. Note that a gamma ray from the source will propagate a certain distance, $d_{\gamma 0}$ and then pair produce. So the pair production points also lie on a sphere of radius $d_{\gamma 0}$. This is partly enforced by the law of sines in Eq. (10), which gives a relation between δ and θ . The intersection of this sphere and the PP surface define a one-dimensional curve in space; CMB photons that are inverse Compton scattered along the one-dimensional curve can propagate to Earth. However, not all points on this one-dimensional curve will satisfy the final constraint. Namely, Eq. (12), picks out a limited set of points on the one-dimensional curve and these give the trajectories of the gamma rays that are observed.

The PP surface can be found analytically for simple cases. For instance, the constraint in Eq. (17) with the helical magnetic field from Eq. (23), which has $b_z = 0$, reduces to,

$$b_\rho \cos(\delta/2 - \theta) = 0, \quad (24)$$

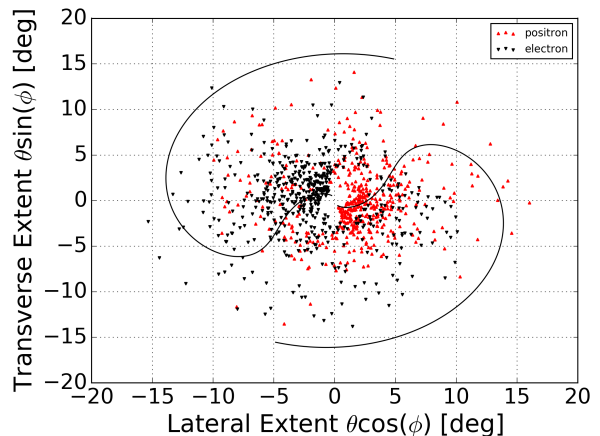
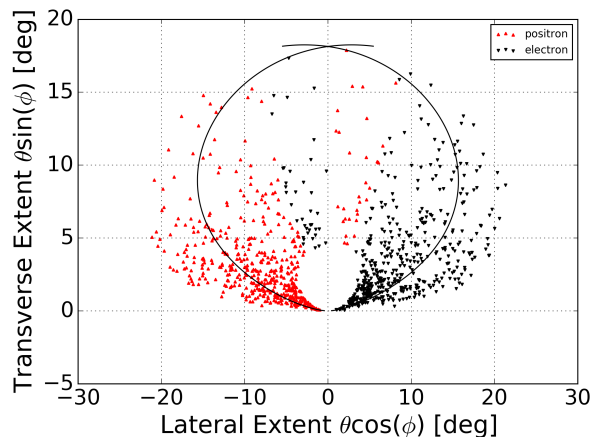


FIG. 3: Same as in Fig. 2 but now red (black) points originate from inverse Compton scattering due to positrons (electrons). If the source was taken to emit along a jet, most of the observed gamma rays would originate from either positron or electron processes but not both.

with

$$b_\rho = \mathbf{B} \cdot \hat{\rho} = \sin(2\pi z/\lambda + \phi). \quad (25)$$

As $\cos(\delta/2 - \theta) = 0$ has only one solution at $\delta = \pi$, $\theta = 0$ in the physical range $\theta \in [0, \pi/2]$, $\delta \in [0, \pi]$, the surface is mainly determined by $b_\rho = 0$ which translates to,

$$\phi = -\frac{2\pi z}{\lambda}. \quad (26)$$

This equation describes a spiral structure as seen in Figure 4.

Until now, we have been assuming that the source emits photons isotropically. Below, we will also consider the case when the source emits photon in a collimated jet. In that case, there is a fourth constraint restricting the relevant part of the PP surface to where it intersects the jet, and it is quite possible that there is no solution. We ignore such cases as they are observationally irrelevant.

In following figures we will show PP locations, even if they do not lie within the jet. Only those PP locations that lie within the jet will lead to observed gamma rays.

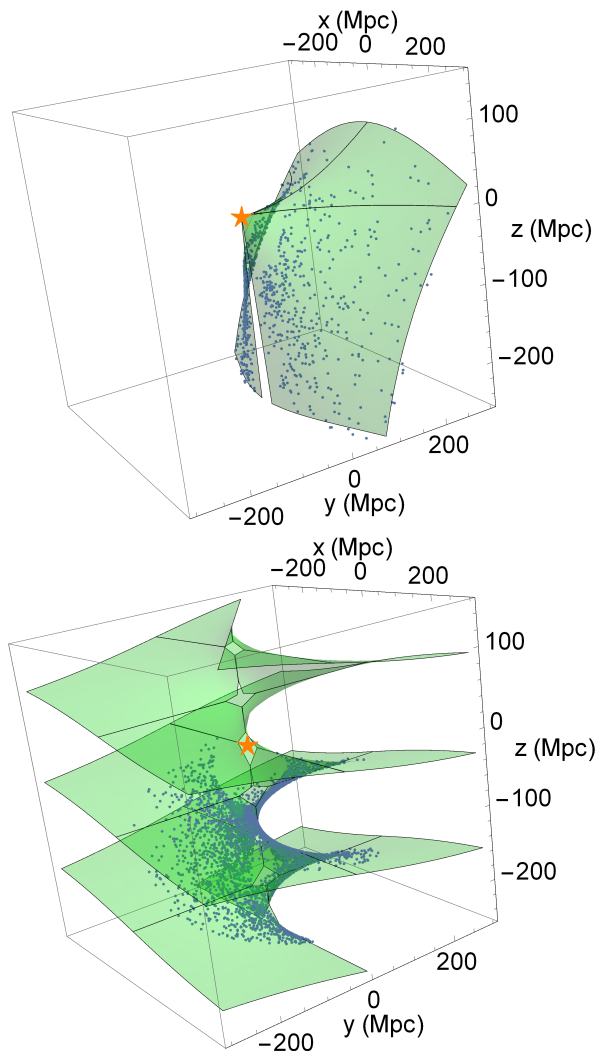


FIG. 4: The PP surface for the uniform magnetic field of Eq. (22) (top) and the maximally helical magnetic field of Eq. (23) (bottom). The source is located at the orange star; the observer is at $z = -1$ Gpc. The blue points are the events that give rise to the halos shown in Figs. 2.

Fig. 5 presents an example in which the source has a jet with half-opening angle $\theta_{\text{jet}} = 5^\circ$ and the magnetic field is given by Eq. (23). The jet direction is chosen so that the Earth lies within the cone of the jet and the blazar can be seen directly. The top plots in both figures show that the jet picks out a small region of the PP surface, and the bottom plots show the resulting halo.

IV. PARAMETER DEPENDENCE OF HALO

In this section we discuss the structure of the halo as the parameters B_0 , λ and the sign of the helicity of the maximally helical magnetic field in Eq. (23) are varied. The concept of the PP surface will be a useful tool for this discussion as it allows us to clearly see how the magnetic

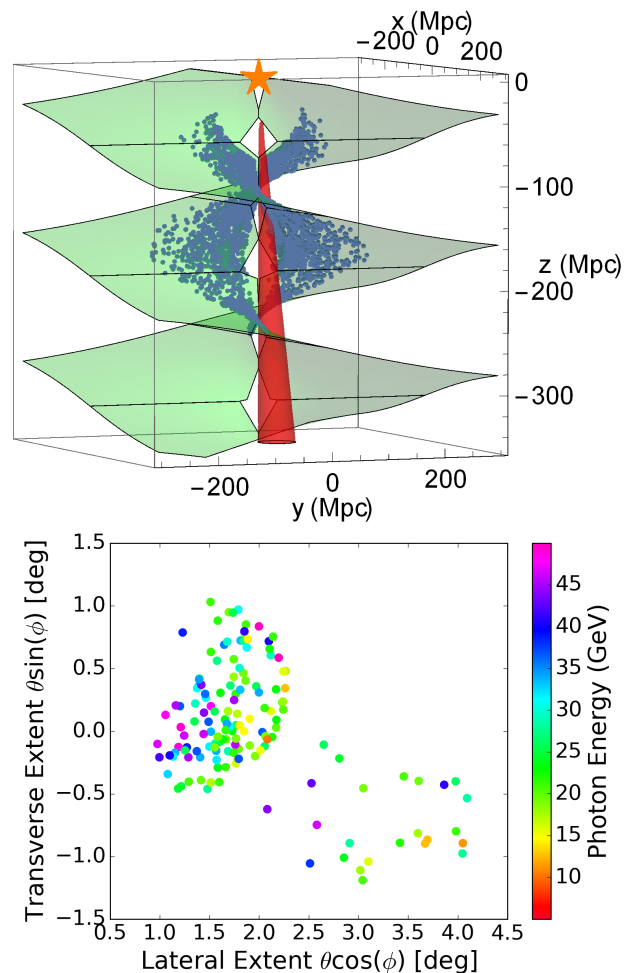


FIG. 5: Example of how a blazar with a jet will only shine and activate a small region of the PP surface (top) and the resultant halo (bottom). The magnetic field is given in Eq. (23) with $B_0 = 10^{-14}$ G, $\lambda = 250$ Mpc.

field dictates the halo's shape.

The magnetic field strength directly affects the amount of bending of the lepton trajectories since the gyroradius $R_L \propto 1/B_0$. Therefore a weak magnetic field will require that the initial TeV gamma ray is already propagating nearly towards Earth. Thus reducing B_0 will shrink the size of the halo at any given gamma ray energy, although lower energy gamma rays may now enter the field of view. This can be seen in Fig. 6 which was created using $B_0 = 5 \times 10^{-15}$ G and $\lambda = 250$ Mpc. The plot looks almost identical to Fig. 5, which was created using $B_0 = 10^{-14}$ G, except that the extent of the halo in the x and y directions, for photons of the same energy, has shrunk by a factor of ~ 2 . If one does not track the photon's energy, the effect of a change in B_0 is not easily seen through the morphology of the halos as their shapes and sizes are determined by the intersection of the jet and the PP surface. We show a few example of this interplay in the sketch of Fig. 7. It is then possible to learn valuable information about the inter-galactic magnetic field

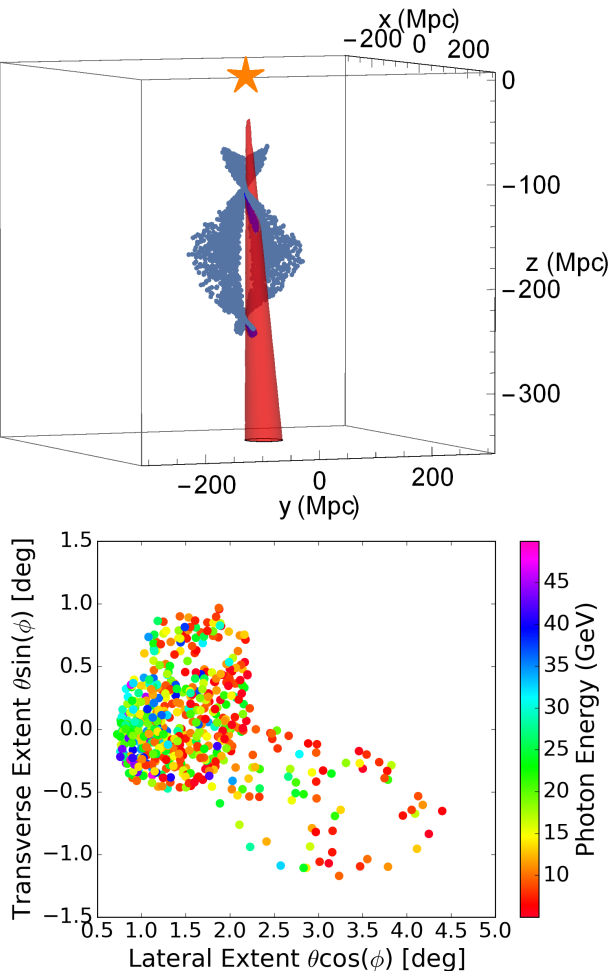


FIG. 6: Monte Carlo simulation with stochastic PDs using the magnetic field of Eq. (23) and with the same setup as in Fig. 5 but with B_0 reduced to $5 \times 10^{-15} G$. Compared to Fig. 5, we see that the high energy gamma rays (blue points) are more clustered and so the halo size is smaller at fixed energy. However, the reduced field strength also causes lower energy gamma rays to come into the field of view, and the overall halo size does not change due to a reduced B_0 .

in the region of the PP locations by observing the halo's shape. In a real situation, we cannot observe the full halo shape as it will be contaminated by background photons coming from other sources. However, we can still extract certain useful halo information since the background is expected to be stochastically isotropic and certainly not parity odd.

As can be seen from Eq. (3), the MFP $D_{\gamma_0}^c$ of the TeV photons are of the order of 10 – 100 Mpc. Any magnetic field with coherence length much larger than $D_{\gamma_0}^c$ will appear constant in space. On the other hand, for $\lambda_c \ll D_{\gamma_0}^c$, the halo will be produced from a rapidly varying part of the PP surface and will be more scattered.

The helicity of the magnetic field in Eq. (23) can be flipped by changing $x \rightarrow -x$. A flip in the helicity simply leads to a parity inversion of the PP surface and the

halo spiral also changes handedness. However, to get more statistics, we will investigate both helicities using independent simulations in Sec. V.

V. Q STATISTIC: ANALYTICAL MAGNETIC FIELDS

One of the main goals of this work is to determine if the helicity of the inter-galactic magnetic field can be deduced from the shape of the blazar halos. As we have seen, under certain conditions, a helical inter-galactic magnetic field can produce a clear spiral-like structure in a gamma ray halo. Hence it is important to develop a statistical technique that is sensitive to this structure. A statistic, called Q , was developed in Ref. [17], and was applied to the *diffuse* gamma ray background observed by the Fermi telescope in Refs. [4, 5]. A non-zero value of Q was observed with high confidence in comparison to Monte Carlo simulations that assume no inter-galactic magnetic field.

One can see from the halo plots above, *e.g.* Fig. 2, that the arrival direction of high energy photons tend to be closer to the blazar line-of-sight than those for lower energy photons. This is mainly due to the smaller magnetic bending at higher energies. Hence different locations of the PP surface are sampled by photons of different energies and the observed gamma rays can carry an imprint of any curvature or twist of the PP surface. More precisely, the work of Ref. [17] showed that a left (right) handed helical magnetic field will create left (right) handed spiral patterns in the observed photons.

Below we briefly review the idea behind a slightly modified version of the Q statistic proposed in Ref. [17]. We will apply the statistics on regions surrounding an observed blazar whose angular position will be denoted by the unit vector $\mathbf{n}^{(3)} = \hat{\mathbf{z}}$. We consider a disk of radius R centered on the location of the source and consider the set of photons within this disk. These photons are binned according to their energies into non-overlapping bins ΔE_1 , ΔE_2 . We use N_i to denote the number of photons in bin ΔE_i within the disk of radius R . We then perform the sum,

$$Q(\Delta E_1, \Delta E_2, R) = \frac{1}{N_1 N_2} \sum_{i=1}^{N_1} \sum_{j=1}^{N_2} \mathbf{n}_i^{(1)} \times \mathbf{n}_j^{(2)} \cdot \mathbf{n}^{(3)} \Theta(\mathbf{m}_i^{(1)} \cdot \mathbf{m}_j^{(2)}) \quad (27)$$

where $\mathbf{n}_i^{(a)} \equiv \mathbf{n}_i(\Delta E_a)$ is the unit vector denoting the arrival direction of photon i in bin a ; $\mathbf{m}_i^{(a)}$ is the unit vector obtained by projecting $\mathbf{n}_i^{(a)}$ on to the xy-plane: $\mathbf{m}_i^{(a)} = \mathbf{n}_i^{(a)} - (\mathbf{n}_i^{(a)} \cdot \hat{\mathbf{z}})\hat{\mathbf{z}}$. The original Q statistic in Ref. [17] was defined without the Heaviside function (Θ) in Eq. (27).

We find that the Θ factor improves the resolution of Q . Without the Θ factor, the Q -statistic is determined by the cross product of the *average* arrival direction of

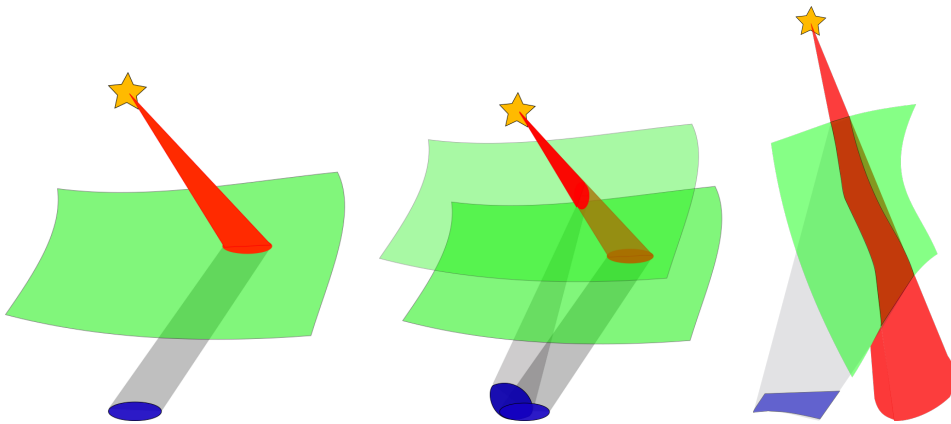


FIG. 7: Sketch of a blazar jet shown in red intersects the green PP surface which delimits the shape of the halo (shown in blue) as seen by some observer. The halo photons must be distributed in the blue region. A situation similar to the one depicted in the middle and third sketch can be seen from the simulations in Fig. 5 and Fig. 8 below. The differences between the many possible shapes arise due the characteristics of the intersection between the blazar’s jet and the PP surface.

the photons (in two energy bins) within a radius R of the source. Because of the electron-positron symmetry, photons tend to arrive on either side of the source (see Fig. 3), and the average arrival direction tends to be near the origin. Introducing the Θ factor ensures that for every high energy photon selected, we only average the low energy photons that arrive on the same side with respect to the source. Then there is a larger contribution to the value of Q . Essentially the Θ term limits the sum to gamma rays within the electron (or the positron) branch of the halo (see Fig. 3). We illustrate the Q -statistic in Fig. 9.

In the presence of background gamma rays in addition to the blazar gamma rays, we expect $Q(R)$ to start near 0 at $R = 0$, grow to a peak value near $R = R_{\text{halo}}$, where R_{halo} is the angular radius of the halo, and finally come back down towards 0 at large R where the signal becomes background dominated. However in mock maps with no background, the value of Q should asymptotically flatten out to its maximal value attained at R_{halo} , and its value will be negative (positive) for right (left) handed magnetic fields. We can see this behavior in Fig. 10 where we simulate the halo without any stochasticity and with the magnetic field of Eq. (23).

To showcase the Q -statistic in this paper we will separate the gamma rays in three energy bins:

$$\Delta E_1 = (5, 20), \quad \Delta E_2 = (20, 35), \quad \Delta E_3 = (35, 50), \quad (28)$$

all numbers in GeV.

VI. Q STATISTIC: STOCHASTIC MAGNETIC FIELDS

The clean result of Fig. 10 will get noisy once we include stochastic magnetic fields and stochastic PDs. Indeed, a randomly generated magnetic field can sometimes

create halos whose Q -statistics suggest the wrong helicity. It is therefore important to average over many realizations of the magnetic field and the jet orientation. Each realization will simulate a blazar with a jet of half-opening angle $\theta_{\text{jet}} = 5^\circ$ and having Earth in its LoS. The jet is also constrained to generate a halo with at least 3 events in order for the statistics to be applied; this condition is generally automatically satisfied if Earth is in the jet’s LoS and the root mean squared magnetic field strength satisfies $B_0 \leq 10^{-14}\text{G}$. Larger values of B_0 create too much bending and very few, if any, upscattered photons reach Earth from seen blazars. Jets pointing further away from the LoS might still yield observable photons but we would not be able to identify these blazars. This bending is also the reason for the empty regions around the axis of the PP surface seen in Fig. 5. The empty region gets larger for larger B_0 .

We will consider magnetic fields of the form,

$$\mathbf{B}(\mathbf{x}) = \frac{1}{2N^2 + 2} \sum_{\mathbf{k} \in K} \mathbf{b}(\mathbf{k}, f_{\text{H}}, B_{\text{rms}}) e^{i\mathbf{k} \cdot \mathbf{x}} \quad (29)$$

with the set K consisting of $2N^2 + 2$ vectors which have magnitude k_{mag} and whose directions are approximately uniformly spread over the unit sphere. Half of the Fourier coefficients $\mathbf{b}(\mathbf{k}, f_{\text{H}}, B_{\text{rms}})$ are drawn from their respective distribution as outlined in Appendix A, while the other half are set by the requirement $\mathbf{b}(\mathbf{k}, f_{\text{H}}, B_{\text{rms}}) = \mathbf{b}^*(-\mathbf{k}, f_{\text{H}}, B_{\text{rms}})$, necessary for obtaining a real value for the magnetic field. The value of $-1 \leq f_{\text{H}} \leq 1$ controls the handedness of the field, namely $f_{\text{H}} = 1$ (-1) corresponds to a maximally right-handed (left-handed) helical field. Finally B_{rms} determines the root mean square of $\mathbf{B}(\mathbf{x})$.

In Fig. 12 we compute the Q -statistics for 100 realizations of halos created with canonical PDs and with a

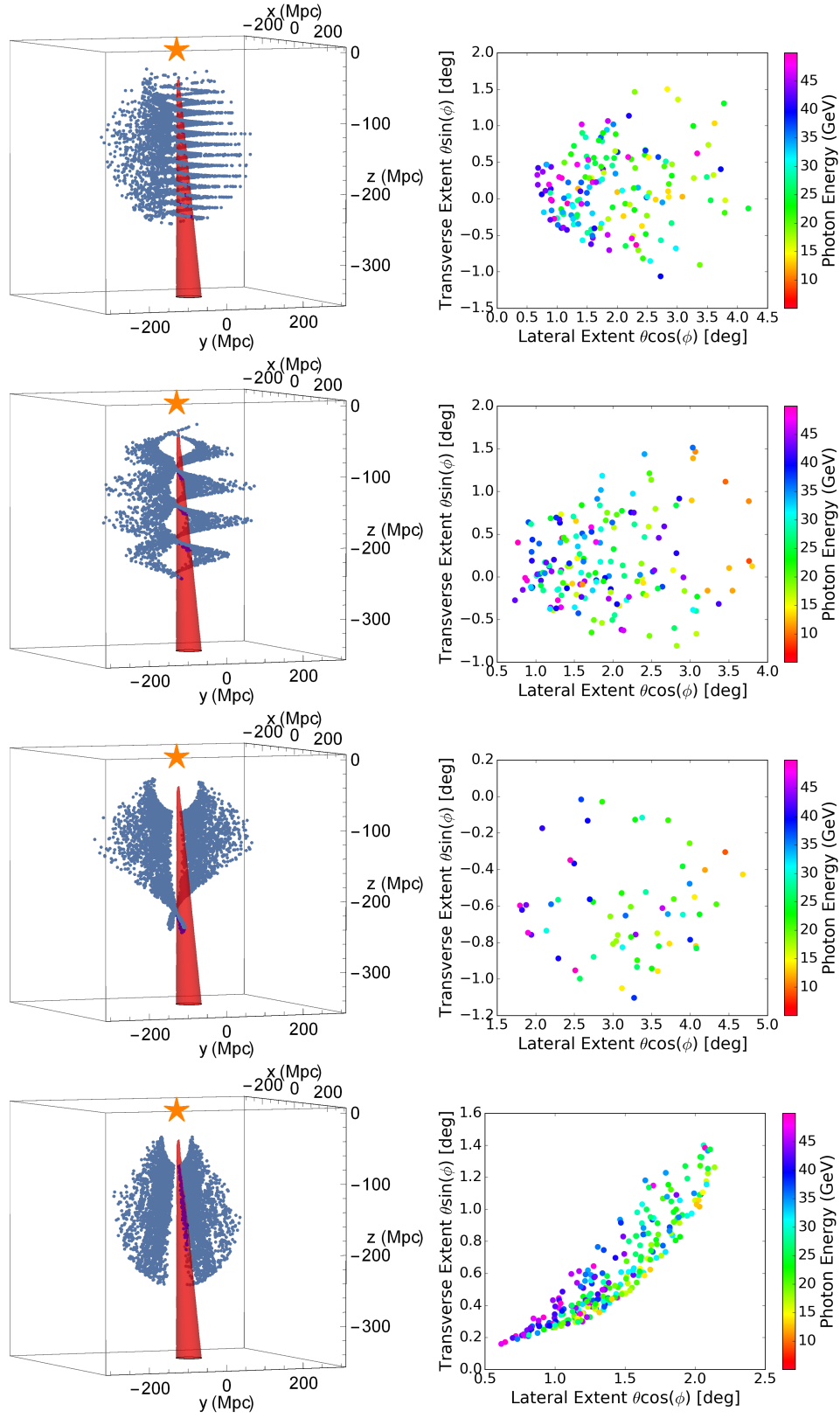


FIG. 8: The PP locations on the PP surface and jet (left) and corresponding halo (right) for $\lambda = 30, 100, 500, 2000$ Mpc for the magnetic field in Eq. (23) with $B_0 = 10^{-14}$ G. The direction to the source is at $\theta = 0$.

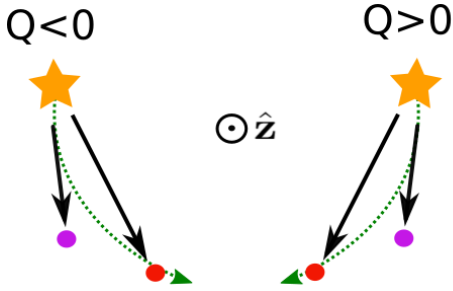


FIG. 9: Illustration of the Q -statistic. The plot represents two blazar halos in the observational plane, each halo with just two photons, one at high energy (purple) and the other at low energy (red). The image of the blazars is denoted by the stars and the line of sight to the blazar (along $\hat{\mathbf{z}}$) points out of the plane of the page as denoted by the arrow tip. The left sketch shows a situation where $Q < 0$ since $\mathbf{n}_{\text{red}} \times \mathbf{n}_{\text{purple}} \cdot \mathbf{n}_{\text{blazar}} < 0$; similarly the sketch of the blazar on the right shows a $Q > 0$ situation.

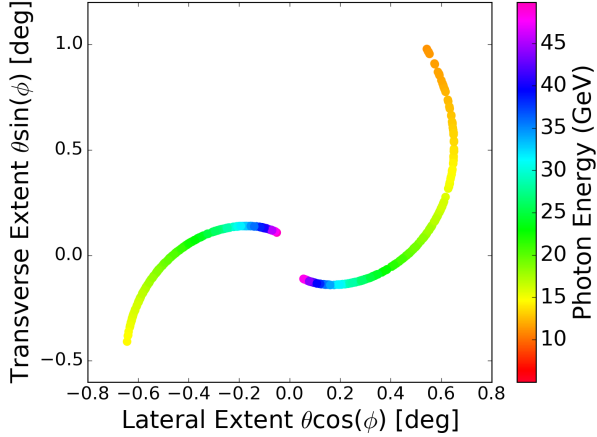


FIG. 10: A set of simulated observed photons from the halo formed by a blazar's jet with half-opening angle of 5° . This simulation did not include any stochasticity in the mean free path of the TeV γ -ray or the pair produced leptons, as such the energy of the photons are in one-one correspondence with their propagation distance. The surrounding magnetic field is given by Eq. (23) with $B_0 = 2 \times 10^{-15}$ G and $\lambda = 250$ Mpc.

random magnetic field created using the parameters

$$\begin{aligned} B_{\text{rms}} &= 2 \times 10^{-15} \text{ G}, \quad k_{\text{mag}} = 0.01/\text{Mpc}, \\ f_H &= +1, \quad 2N^2 + 2 = 27, \end{aligned} \quad (30)$$

where $2N^2 + 2$ is the number of directions of the \mathbf{k} vector in Eq. (29). In Fig. 13 we plot the average of Q over all the realizations, denoted $\bar{Q}(R)$, for the same runs as in Fig. 12 and for the three gamma ray energy bin combinations. By doing so, we have in mind of averaging the Q -statistics obtained from small regions around multiple observed blazars. The plot also shows the standard error in $\bar{Q}(R)$ which is given by the standard deviation of $Q(R)$ divided by the square root of the number of real-

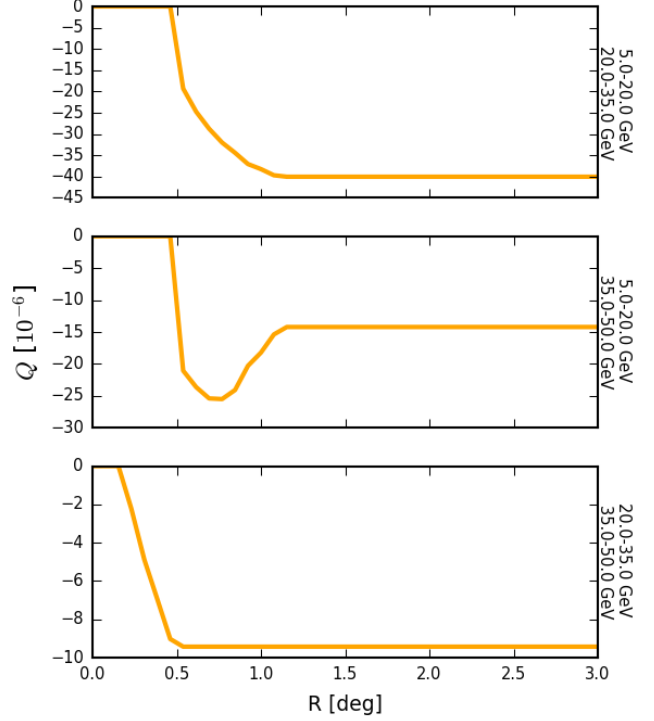


FIG. 11: The result of applying the Q -statistic to the observed photons in Fig. 10. The curves start at $R \sim 0.5^\circ$ because there are insufficient photons within that distance.

izations in the Monte Carlo simulations. The standard error follows from the central limit theorem and is the error in using the sample mean to estimate the population mean. However, it assumes that the samples, Monte Carlo simulations in our case, from which values of $Q(R)$ are drawn are independent and identically distributed. This is certainly true in our setup but may not be true for actual observations in which the same photons might contribute to the $Q(R)$ calculated for blazars that are close to each other. In addition, there will be variation in the distance to observed blazars and other source characteristics. We plan to take some of these factors into account in a follow-up analysis.

It is very clear from Fig. 13 that \bar{Q} is a good measure of the magnetic field helicity when we assume canonical PDs. The next step is to see if \bar{Q} remains a useful discriminant of magnetic helicity, even after we include stochasticity in both the magnetic field and the PDs. We have plotted $\bar{Q}(R)$ versus R for 1000 Monte Carlo simulations for $f_H = 0, \pm 1$ (Fig. 14). The plots show a clear correlation between $\bar{Q}(R)$ and the helicity of the magnetic field. It is also reassuring that the $f_H = +1$ plot is the mirror image of the $f_H = -1$ curve, just as we would expect due to parity reflection.

Next we examine the dependence of $\bar{Q}(R)$ on magnetic field parameters. In Fig. 15 we plot $\bar{Q}(R)$ for sev-

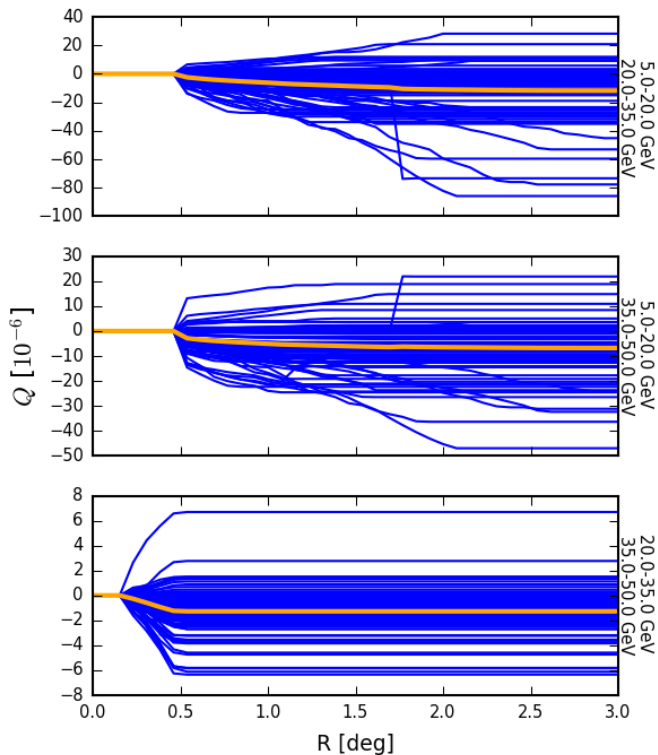


FIG. 12: $Q(R)$ versus R for 100 Monte Carlo runs when the stochastic magnetic fields are generated using the parameters shown in Eq. (30) with $f_H = +1$ and canonical PDs. The mean $\bar{Q}(R)$ is shown by the orange curve.

eral different magnetic field strengths and for fixed helicity $f_H = 1$. We see that increasing the magnetic field strength leads to an increasing amplitude of \bar{Q} for *all* energy combinations. The increase is due to the magnitude of $\mathbf{n}_1 \times \mathbf{n}_2$ which becomes larger as the bending allows $\mathbf{n}_1, \mathbf{n}_2$ to point further apart.

The effect of changing the magnetic field coherence scale is shown in Fig. 16 where the magnetic field strength and other parameters are fixed and only k_{mag} is varied. The magnetic field with larger coherence length gives a larger signal, but there is a turning point as extremely large coherence scale fields will behave like uniform fields. The signal for smaller correlation length is washed out but the suppression depends on the energy combination. This is to be expected from the analysis of Ref. [17] since \bar{Q} with a certain energy combination is sensitive to the magnetic helicity power spectrum at a definite coherence scale that is determined by the combination of energies. To probe magnetic fields on small length scales, it is necessary to consider gamma rays whose energies are close together [17]. Thus the energy bins also have to be smaller and this means that the statistics is poorer.

The above results are from 1000 realizations in the Monte Carlo simulations. Each run gives a certain

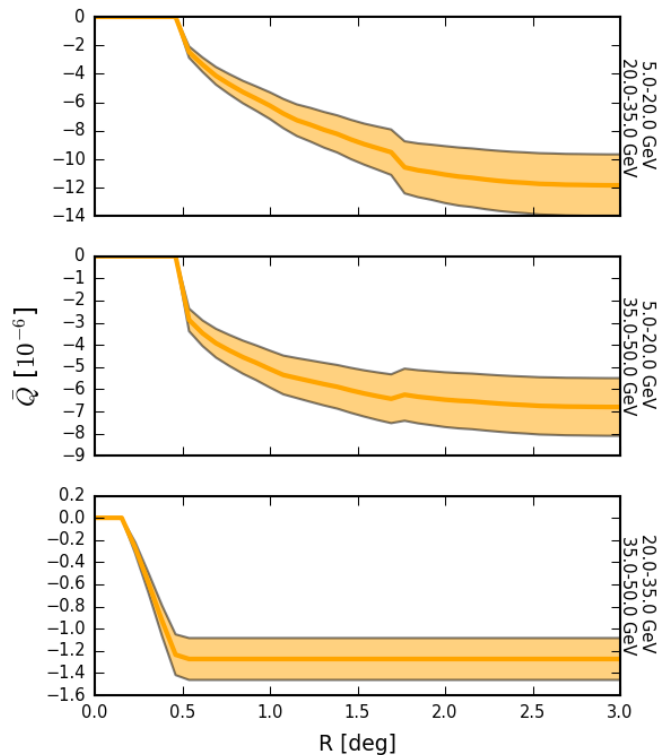


FIG. 13: A zoomed-in view of $\bar{Q}(R)$ of Fig. 12 for stochastic magnetic fields and canonical PDs. The width of the error band is given by the standard error *i.e.* standard deviation of the 100 Monte Carlo $Q(R)$ values divided by the square root of the sample size (100).

asymptotic value $\bar{Q}(R_{\text{max}})$. The 1000 values of $\bar{Q}(R_{\text{max}})$ for different magnetic field helicities and for different energy combinations are plotted in histograms in Fig. 17. Non-vanishing helicity causes the distribution of $\bar{Q}(R_{\text{max}})$ to skew in a direction that is in correspondence with the sign of the helicity.

VII. THE BUMP AT SMALL R

The Q-statistic is essentially a measure of the differential rotation found in the arrival direction of photons of different energies. Q will be negative (positive) if the rotation is right (left)-handed as is depicted in Fig. 9. The results of our Monte Carlo simulations, for example in Fig. 14, show that \bar{Q} has a bump at small R . Here we provide an explanation of this small R bump.

First note that the small R bump does not appear in Fig. 13 that was produced by assuming canonical, not stochastic, PDs. Therefore the appearance of the bumps must be tied to the stochasticity of the PDs. When the PDs take their canonical values, low energy gamma rays arise from interactions on a region of the PP surface that

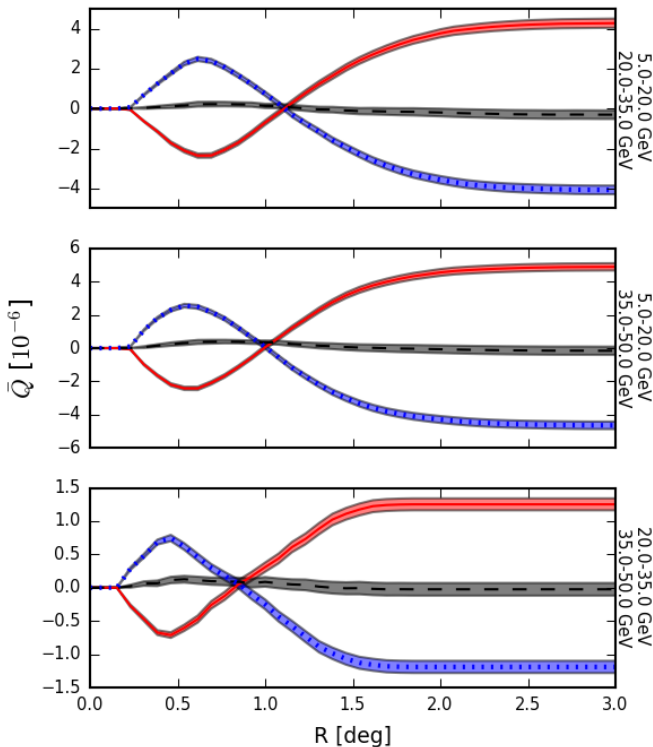


FIG. 14: $\bar{Q}(R)$ versus R for $f_H = -1$ (red, solid), $f_H = 0$ (black, dashed) and $f_H = +1$ (blue, dotted) for the three energy bin combinations: $(\Delta E_1, \Delta E_2)$ (top row), $(\Delta E_1, \Delta E_3)$ (middle row) and $(\Delta E_2, \Delta E_3)$ (bottom row) where the bins are defined in Eq. (28). The other parameters for the stochastic magnetic fields are given in Eq. (30); the PDs are also stochastic as described in Sec. III. The bands denote standard error of \bar{Q} .

is far from the source, whereas high energy gamma rays arise closer to the source. Hence the PP locations are distributed in a natural progression, from close to the source to further away from the source, as the energy of the photons is decreased. This can be seen in Fig. 18. On the other hand, when the PDs are stochastic, the low energy photons can arise from close to the source and also from far away as seen in Fig. 19. The ones that come from close to the source are also closer to the LoS due to the geometry of the jet and are observed at smaller values of R . These low energy photons bend more than the high energy photons and can have PP locations that are higher up along the LoS than the high energy photons. Hence they measure the twist of the PP surface as one traverses the PP surface from low positions along the LoS to high positions (instead of the usual direction of traversal from high to low). If R is large, then the Q statistics takes into account all the low energy photons and these are predominantly far away from the source. So at large R , the sign of the Q statistics is the same as that in the case of canonical PDs. Thus $Q(R)$ changes sign once R is large enough so that the mean position

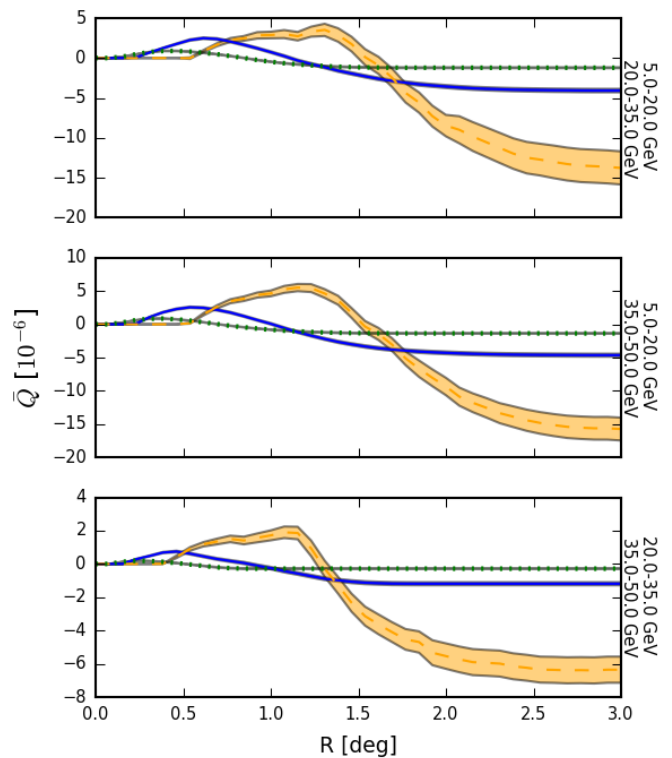


FIG. 15: \bar{Q} versus R for 1000 simulations with $B_{\text{rms}} = 10^{-15}$ G (green, dotted), 2×10^{-15} G (blue, solid), and 5×10^{-15} G (orange, dashed) and $f_H = 1$, $k = 0.01/\text{Mpc}$.

of the PP locations of the low energy photons is below that of the high energy photons. This effect results in a halo of the form seen in Fig. 20 and translates into a bump in $Q(R)$ at small values of R and with a sign that is opposite to that of the asymptotic value of Q .

VIII. CONCLUSIONS

We have studied the effect of stochastic inter-galactic magnetic fields on the morphology of gamma ray halos. The dependence of the morphology on the magnetic field strength, the coherence length, and the helicity were investigated. Most importantly, we have provided an understanding of the structure of the halo in geometrical terms, as arising due to the ‘‘PP surface’’ as determined by the magnetic field. In simple cases, the PP surface can be found analytically (for example, Eq. (26)).

To analyze the halo morphology, we have proposed a sharper version of the Q -statistic in Eq. (27) and applied it to simulated halos. Our key finding is that Q is a powerful diagnostic of the magnetic helicity (Fig. 14), field strength (Fig. 15) and coherence scale (Fig. 16). Based on the analytical work of Ref. [17], we expect the sensitivity of Q to the coherence scale to depend crucially on the energies of the gamma rays that are used. It would be interesting to quantitatively examine how the

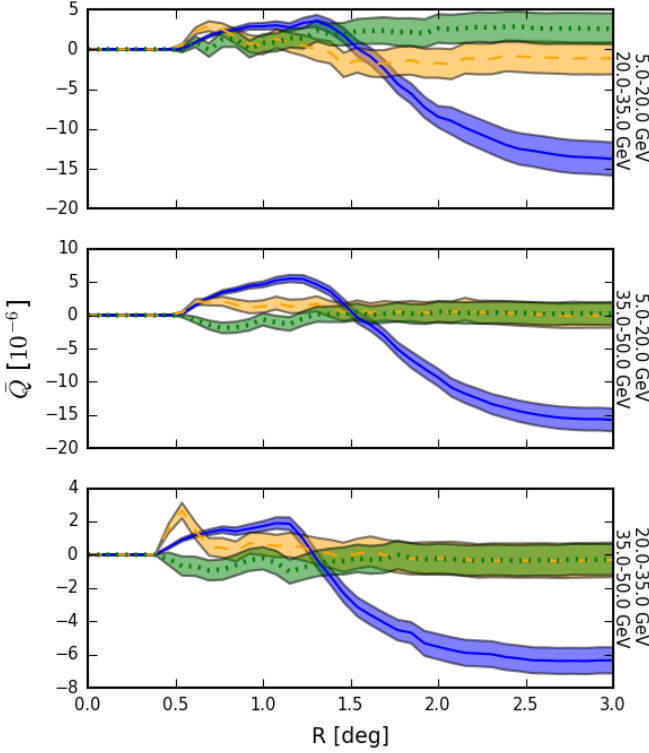


FIG. 16: \bar{Q} versus R for 1000 simulations with $k = 0.01/\text{Mpc}$ (solid, blue), $k = 0.1/\text{Mpc}$ (orange, dashed), $k = 1/\text{Mpc}$ (green, dotted) with $B_{\text{rms}} = 2 \times 10^{-15}$ G and $f_H = +1$.

sensitivity of Q to the coherence scale can be improved with a choice of energy bins.

In addition, our Monte Carlo simulations have revealed a bump in $\bar{Q}(R)$ at small values of R (see Fig. 14). We have understood and explained this feature in terms of the PP surface in Sec. VII. This new feature may become useful in the analysis of real data in the future.

Our present study is limited in a few ways that we plan to overcome in future work. First, we have not included any background gamma rays. These will introduce noise in the evaluation of \bar{Q} and the error bars will increase. We have also limited ourselves to stochastic isotropic magnetic fields but with only one $|\mathbf{k}|$ -mode. This is useful at this stage as it allows us to diagnose the effects of changing the coherence scale. In future, we plan to include a spectrum of the magnetic field as motivated by current observations [11]. In future we also plan to incorporate the full development of the electromagnetic cascade into our numerical code, perhaps along the lines of Ref. [14] or [16]. Once we have understood individual blazar halos, we will apply our techniques to the diffuse gamma ray background which is expected to contain halos due to unseen blazars as well as those due to identified blazars.

Acknowledgments

We thank Andrew Long for comments. TV is supported by the U.S. Department of Energy, Office of High Energy Physics, under Award No. DE-SC0013605 at ASU.

Appendix A: Generation of Isotropic Random Magnetic Fields

To generate helical magnetic fields, we first decompose the magnetic field $\mathbf{B}(\mathbf{x})$ in circularly polarized modes with basis vectors $\mathbf{K}^\pm(\mathbf{k})$ that are divergence-free eigenfunctions of the Laplace operator

$$\mathbf{K}^\pm(\mathbf{k}) = \mathbf{e}^\pm(\mathbf{k})e^{i\mathbf{k}\cdot\mathbf{x}} \equiv \frac{\mathbf{e}_1(\mathbf{k}) \pm i\mathbf{e}_2(\mathbf{k})}{\sqrt{2}}e^{i\mathbf{k}\cdot\mathbf{x}}. \quad (\text{A1})$$

The triad of unit vectors, $\{\mathbf{e}_1, \mathbf{e}_2, \mathbf{e}_3\}$, is constructed as

$$\mathbf{e}_1 \equiv \frac{\mathbf{n}_0 \times \hat{\mathbf{k}}}{|\mathbf{n}_0 \times \hat{\mathbf{k}}|}, \quad \mathbf{e}_2 \equiv \frac{\hat{\mathbf{k}} \times \mathbf{e}_1}{|\hat{\mathbf{k}} \times \mathbf{e}_1|}, \quad \mathbf{e}_3 \equiv \frac{\mathbf{k}}{k} \equiv \hat{\mathbf{k}} \quad (\text{A2})$$

where \mathbf{n}_0 is any chosen unit vector such that $\mathbf{n}_0 \neq \hat{\mathbf{k}}$.

With these definitions, the \mathbf{e} 's form a right-handed orthonormal system and we have,

$$\nabla \cdot \mathbf{K}^\pm = 0, \quad \nabla \times \mathbf{K}^\pm = \pm k\mathbf{K}^\pm, \quad \mathbf{K}^{\pm*}(\mathbf{k}) = -\mathbf{K}^\pm(-\mathbf{k}) \quad (\text{A3})$$

Hence any magnetic field can be decomposed as,

$$\begin{aligned} \mathbf{B}(\mathbf{x}) &= \int \frac{d^3k}{(2\pi)^3} \mathbf{b}(\mathbf{k})e^{i\mathbf{k}\cdot\mathbf{x}} \\ &= \int \frac{d^3k}{(2\pi)^3} [b^+\mathbf{K}^+ + b^-\mathbf{K}^-], \end{aligned} \quad (\text{A4})$$

with the condition that

$$b^{\pm*}(\mathbf{k}) = -b^\pm(-\mathbf{k}) \quad (\text{A5})$$

to ensure that $\mathbf{B}(\mathbf{x})$ is real. The divergence-free condition, $\nabla \cdot \mathbf{B} = 0$, is automatically satisfied in this procedure.

We are interested in generating random magnetic fields with given energy ($E_B(k)$) and helical ($H_B(k)$) power spectra. The relations between the modes $b^\pm(\mathbf{k})$ and the power spectra are given by

$$\frac{1}{8\pi} \langle |\mathbf{B}(\mathbf{x})|^2 \rangle = \int \frac{k^2 dk}{16\pi^3} [|b^+|^2 + |b^-|^2] \equiv \int E_B(k) d\ln(k) \quad (\text{A6})$$

and

$$\langle \mathbf{A}(\mathbf{x}) \cdot \mathbf{B}(\mathbf{x}) \rangle = \int \frac{k dk}{2\pi^2} [|b^+|^2 - |b^-|^2] \equiv \int H_B(k) d\ln(k). \quad (\text{A7})$$

The ratio of E_B and H_B will be written in terms of a function $f_H(k)$ as [8],

$$H_B(k) = f_H(k) \frac{8\pi}{k} E_B(k), \quad (\text{A8})$$

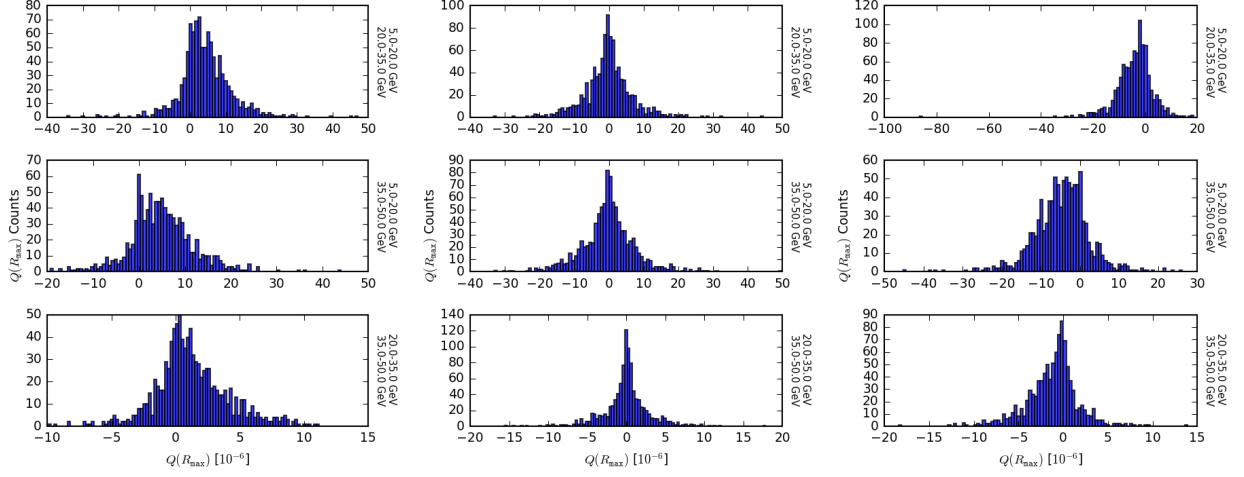


FIG. 17: Histograms of $\bar{Q}(R_{\max})$ for 1000 simulations with parameters quoted in Eq. (30). The histograms are skewed to the right ($\bar{Q} > 0$) for $f_H = -1$ (left column), are symmetric for $f_H = 0$ (central column), and skewed to the left ($\bar{Q} < 0$) for $f_H = +1$ (right column).

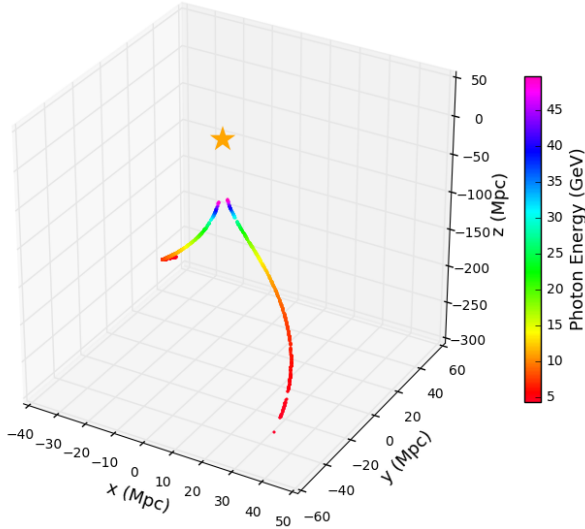


FIG. 18: PP locations of the events for an $f_H = -1$ magnetic field and canonical PDs. The lower the energy of the observed photon, the further away is the PP location from the source.

and the “realizability condition” leads to the restriction

$$-1 \leq f_H(k) \leq 1 \quad (\text{A9})$$

The field is non-helical if $f_H = 0$, maximally right-handed if $f_H = +1$, and maximally left-handed if $f_H = -1$.

Eqs. (A6), (A7) and (A8) allow us to write,

$$|b^\pm|^2 = \left(\frac{2\pi}{k}\right)^3 [1 \pm f_H(k)] E_B(k). \quad (\text{A10})$$

Hence the modes $|b^\pm(\mathbf{k})|$ are drawn from a normal distribution with mean $\mu^\pm = 0$ and standard deviation

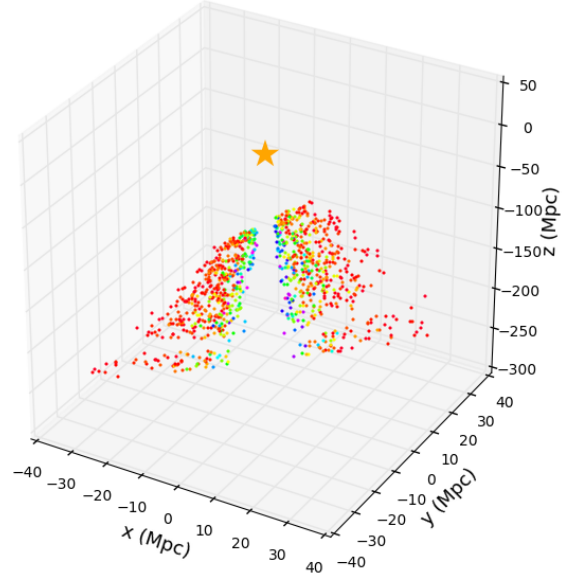


FIG. 19: PP locations of the events for an $f_H = -1$ magnetic field and stochastic PDs. (The corresponding halo is shown in Fig. 20.) The color coding is the same as in Fig. 18. Now the low energy observed photons have PP locations that are spread out in the direction of the LoS and some of these photons (red dots) originate closer to the source than the high energy PP locations (blue dots).

$\sigma^\pm = (1 \pm f_H)(2\pi/k)^3 E_B(k)$. We then include a uniformly drawn phase angle $\theta^\pm(\mathbf{k}) \in [0, 2\pi)$ which yields,

$$b^\pm(\mathbf{k}) = |b^\pm(\mathbf{k})| e^{i\theta^\pm(\mathbf{k})} \quad (\text{A11})$$

In this paper we focus on stochastic magnetic fields that are *isotropic* but have power on a single length scale $\lambda_c = 2\pi/k_{\text{mag}}$ and that have either $f_H(k) = 0$ or $f_H(k) =$

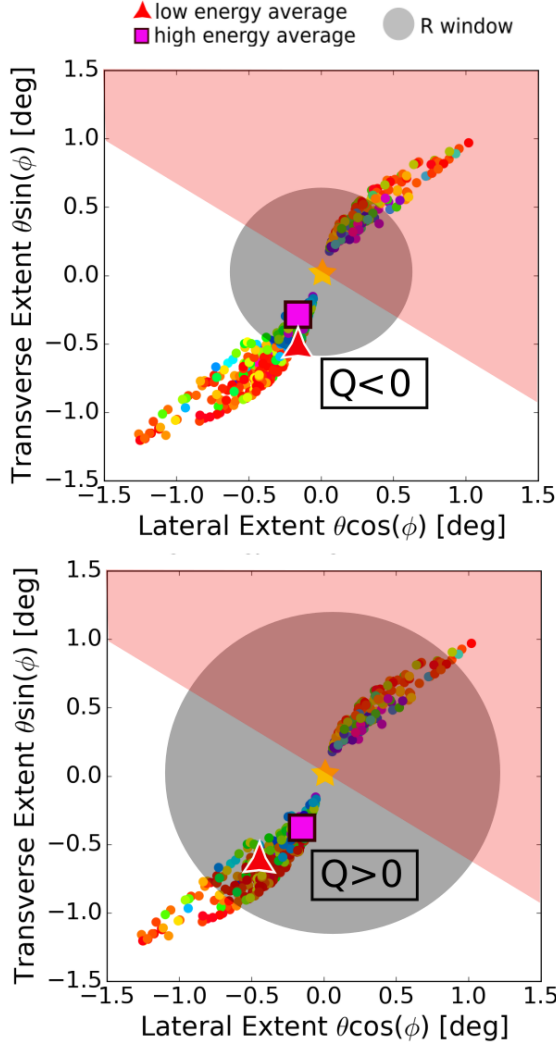


FIG. 20: Halo of a blazar due to a random magnetic field generated with parameters in Eq. (30) but with $f_H = -1$. The Q -statistics is sensitive to half the halo, as depicted by the red shading. Considering the remaining photons in the dark-shaded region, the red triangle and the purple square show the mean arrival directions of the low energy and high energy gamma rays within a disk of small R in the upper diagram and of large R in the lower diagram. Comparing to Fig. 9, we find $Q < 0$ for small R and $Q > 0$ at large R , implying a bump in the $Q(R)$ plot at small R . The color coding is the same as in Fig. 18.

± 1 . This corresponds to a delta function distribution for $E_B(k)$ and vanishing or maximal helicity of either sign. To ensure that the magnetic fields are stochastically isotropic, we choose $N^2 + 1$ vectors \mathbf{k}_n ($n = 1, \dots, N^2 + 1$) that discretize half of the two-sphere of directions in \mathbf{k} -space,

$$\mathbf{k}_n = k_{\text{mag}}(\sin \theta_i \cos \phi_j, \sin \theta_i \sin \phi_j, \cos \theta_i), \quad (\text{A12})$$

with

$$\theta_i = \cos^{-1} \left(\frac{2i-1}{N} - 1 \right), \quad \phi_j = 2\pi \frac{(j-1)}{N}, \quad (\text{A13})$$

for $i, j = 1, \dots, N$, and

$$k_{N^2+1} = k_{\text{mag}}(0, 0, 1) \quad (\text{A14})$$

Once we have \mathbf{k} and $b^\pm(\mathbf{k})$ as described above, we compute

$$\mathbf{b}(\mathbf{k}) = b^+ \mathbf{K}^+ + b^- \mathbf{K}^- \quad (\text{A15})$$

for every $\mathbf{k} = \mathbf{k}_n$. We also find $\mathbf{b}(-\mathbf{k})$ using the reality condition

$$\mathbf{b}(-\mathbf{k}) = \mathbf{b}^*(\mathbf{k}). \quad (\text{A16})$$

Finally we obtain the random magnetic field,

$$\mathbf{B}(\mathbf{x}) = \frac{1}{(2N^2 + 2)} \sum_{\mathbf{k} \in \mathbf{K}} \mathbf{b}(\mathbf{k}) e^{i\mathbf{k} \cdot \mathbf{x}} \quad (\text{A17})$$

where \mathbf{K} is the set of vectors $\{\mathbf{k}_n, -\mathbf{k}_n\}$ for $n = 1, \dots, N^2 + 1$.

[1] A. Neronov and I. Vovk, *Science* **328**, 73 (2010) doi:10.1126/science.1184192 [arXiv:1006.3504 [astro-ph.HE]].
 [2] S. Ando and A. Kusenko, *Astrophys. J.* **722**, L39 (2010) doi:10.1088/2041-8205/722/1/L39 [arXiv:1005.1924 [astro-ph.HE]].
 [3] W. Essey, S. Ando and A. Kusenko, *Astropart. Phys.* **35**, 135 (2011) doi:10.1016/j.astropartphys.2011.06.010 [arXiv:1012.5313 [astro-ph.HE]].

[4] H. Tashiro, W. Chen, F. Ferrer and T. Vachaspati, *Mon. Not. Roy. Astron. Soc.* **445**, no. 1, L41 (2014) doi:10.1093/mnrasl/slu134 [arXiv:1310.4826 [astro-ph.CO]].
 [5] W. Chen, B. D. Chowdhury, F. Ferrer, H. Tashiro and T. Vachaspati, *Mon. Not. Roy. Astron. Soc.* **450**, no. 4, 3371 (2015) doi:10.1093/mnras/stv308 [arXiv:1412.3171 [astro-ph.CO]].
 [6] W. Chen, J. H. Buckley and F. Ferrer, *Phys. Rev. Lett.*

- 115**, 211103 (2015) doi:10.1103/PhysRevLett.115.211103 [arXiv:1410.7717 [astro-ph.HE]].
- [7] J. D. Finke, L. C. Reyes, M. Georganopoulos, K. Reynolds, M. Ajello, S. J. Fegan and K. McCann, *Astrophys. J.* **814**, no. 1, 20 (2015) doi:10.1088/0004-637X/814/1/20 [arXiv:1510.02485 [astro-ph.HE]].
- [8] A. Brandenburg and K. Subramanian, *Phys. Rept.* **417**, 1 (2005) doi:10.1016/j.physrep.2005.06.005 [astro-ph/0405052].
- [9] R. Durrer and A. Neronov, *Astron. Astrophys. Rev.* **21**, 62 (2013) doi:10.1007/s00159-013-0062-7 [arXiv:1303.7121 [astro-ph.CO]].
- [10] J. M. Wagstaff and R. Banerjee, *JCAP* **1601**, 002 (2016) doi:10.1088/1475-7516/2016/01/002 [arXiv:1409.4223 [astro-ph.CO]].
- [11] T. Vachaspati, arXiv:1606.06186 [astro-ph.CO].
- [12] A. Elyiv, A. Neronov and D. V. Semikoz, *Phys. Rev. D* **80**, 023010 (2009) doi:10.1103/PhysRevD.80.023010 [arXiv:0903.3649 [astro-ph.CO]].
- [13] A. J. Long and T. Vachaspati, *JCAP* **1509**, no. 09, 065 (2015) doi:10.1088/1475-7516/2015/09/065 [arXiv:1505.07846 [astro-ph.CO]].
- [14] R. Alves Batista, A. Saveliev, G. Sigl and T. Vachaspati, *Phys. Rev. D* **94**, no. 8, 083005 (2016) doi:10.1103/PhysRevD.94.083005 [arXiv:1607.00320 [astro-ph.HE]].
- [15] A. E. Broderick, P. Tiede, M. Shalaby, C. Pfrommer, E. Puchwein, P. Chang and A. Lamberts, arXiv:1609.00387 [astro-ph.HE].
- [16] T. Fitoussi, R. Belmont, J. Malzac, A. Marcowith, J. Cohen-Tanugi and P. Jean, doi:10.1093/mnras/stw3365 arXiv:1701.00654 [astro-ph.HE].
- [17] H. Tashiro and T. Vachaspati, *Phys. Rev. D* **87**, no. 12, 123527 (2013) doi:10.1103/PhysRevD.87.123527 [arXiv:1305.0181 [astro-ph.CO]].
- [18] P. A. R. Ade *et al.* [Planck Collaboration], *Astron. Astrophys.* **594**, A13 (2016) doi:10.1051/0004-6361/201525830 [arXiv:1502.01589 [astro-ph.CO]].
- [19] A. Neronov and D. Semikoz, *Phys.Rev. D* **80** (2009) 123012, arXiv:0910.1920.
- [20] M. Ackermann *et al.* [Fermi-LAT Collaboration], *Astrophys. J. Suppl.* **222**, no. 1, 5 (2016) doi:10.3847/0067-0049/222/1/5 [arXiv:1508.04449 [astro-ph.HE]].
- [21] M. Ackermann *et al.* [Fermi-LAT Collaboration], *Phys. Rev. Lett.* **116**, no. 15, 151105 (2016) doi:10.1103/PhysRevLett.116.151105 [arXiv:1511.00693 [astro-ph.CO]].